On the efficiency and accuracy of stress integration algorithms for constitutive models based on non-associated flow rule

Author(s):
Hippke, Holger; Manopulo, Niko; Yoon, Jeong Whan; Hora, Pavel

Publication date:
2018-03

Permanent link:
https://doi.org/10.3929/ethz-b-000242806

Originally published in:
International Journal of Material Forming 11(2), https://doi.org/10.1007/s12289-017-1347-6

Int J Mater Form (2018) 11:239–246
DOI 10.1007/s12289-017-1347-6

ORIGINAL RESEARCH

On the efficiency and accuracy of stress integration algorithms for constitutive models based on non-associated flow rule

Holger Hippke[1] · Niko Manopulo[1] · Jeong Whan Yoon[2,3] · Pavel Hora[1]

Received: 12 March 2016 / Accepted: 22 February 2017 / Published online: 20 March 2017

Abstract Constitutive models based on non-associated flow rule enable the accurate description of complex anisotropy phenomena by using distinct, but relatively simple, mathematical description for yield function and plastic potential. The computational complexity of stress integration procedure may thus be significantly reduced. The amount by which this advantage is reflected to the total computation time is, however, a function of the nonlinearity of the problem at hand. The present work aims to make a systematic comparison of two different stress integration algorithms, used in conjunction to non-associated flow rule. A fully explicit and semi-implicit integration scheme are analyzed in terms of accuracy and speed. The implemented yield model is Yld2000-2d with isotropic hardening. The validity of the stress-integration approaches is assessed based on the ability to reproduce stress-ratios, r-values and tensile test results. Additionally, measured earing profiles in cup drawing experiments are compared. The fully explicit implementation shows significant advantages in terms of speed.

Keywords Sheet metal foming · FEM · non-AFR

✉ Niko Manopulo
manopulo@ivp.mavt.ethz.ch

[1] ETH Zurich, Institute of Virtual Manufacturing, Tannenstrasse 3, 8092 Zurich, Switzerland

[2] Faculty of Science, Engineering and Built Environment, Deakin University, Waurn Ponds, VIC 3220, Australia

[3] Department of Mechanical Engineering, KAIST, Daejeon 305-701, Korea

Introduction

Phenomenological constitutive models require the simultaneous satisfaction of the yield condition, consistency condition and the flow rule. A flow rule describes the relationship for an increment in plastic strain and thus possesses an important role in the accuracy of plastic deformation. For metallic materials, which are essentially isochoric under plastic deformation, the plastic strain increment is traditionally assumed to be dependent on (or normal to) the yield surface. This is mainly motivated by the postulation that plastic flow follows the normal to the yield locus and that the yield locus also represents the plastic potential. Furthermore the research as by [9, 15–17] and others, showed that associated flow rule (AFR) guarantees a unique solution of the constitutive equations. The acceptance of AFR has been further strengthened by the work of [8] who derived the associated flow rule from a polycrystalline model under the assumption that Schmidt's law governs plastic deformation.

Many anisotropic yield functions have been proposed and successfully used together with an associated flow rule. An early proposal by [18] is still one of the most widely used models in describing anisotropy for mild steel. Later the research by [19] extended the original formulation for a higher order flow exponent. Barlat and Lian [6] and [3, 5] introduced non-quadratic yield loci based on one linear transformation. Later the Yld2000-2d formulation was introduced by [4], based on two linear transformations. A similar formulation was proposed by [1]. Cazacu et al. [13] introduced an orthotropic asymmetric yield criterion without pressure sensitivity, which was further extended to a strain-rate potential by [14]. Yoon et al. [35] recently sugge sted a pressure sensitive asymmetric yield function formulation.

Non-associated flow rule (non-AFR) based models, which define yield function and plastic potential independently, have been widely used for geotechnical, granular and pressure sensitive materials for decades. Spitzig and Richmond [25] who demonstrated a pressure sensitivity of some steel and aluminum alloys inspired further investigations in this field by [10–12, 27]. Li and Richmond [20] addressed the issue of stability under non-AFR, [28, 29] established the necessary and sufficient conditions to ensure the stability. One of the most important benefits of non-AFR is the additional freedom provided by distinct yield locus and plastic potential. This enables reproducing a complex material behavior using simpler mathematical expressions as proposed by [36] or by the combination of two different functions, as discussed by [26] and [23]. The advantages of non-AFR in predicting earing profiles in cup drawing was thoroughly investigated by [22, 23, 30, 31, 33, 34].

In the scope of this work, an Euler-forward stress integration algorithm [21] and the Euler-backward stress integration method [32] will be systematically investigated for their performances within the framework of non-AFR based models. While Euler-backward formulation is more complicated to be implemented, it remains stable with a larger time step, potentially leading to overall performance gain. On the other hand, Euler-forward integration scheme is stable only for small strain increments an thus more adequate for use in explicit codes with no or limited mass/time scaling. The comparisons have been made using two aluminum alloys. AA5042 whose data was taken from [22] and AA6016, which was characterized at IVP, ETH Zurich. One element tests in different directions are used to validate the efficiency of the integration algorithms, in the absence of external sources of non-linearity. The analysis is then extended to more complex geometries of tensile test and cup drawing tests.

Constitutive model

The constitutive models as well as numerical implementations are discussed in this section. The materials are assumed to be orthotropic, with no strength differential in tension and compression and obeying isotropic hardening. The yield condition can be written as follows:

$$\phi_y(\boldsymbol{\sigma}) - \sigma_y(\bar{\varepsilon}_p) = 0 \tag{1}$$

where ϕ_y is the yield function depending on the Cauchy stress tensor $\boldsymbol{\sigma}$ and σ_y is the yield stress as the function of effective plastic strain $\bar{\varepsilon_p}$. The flow rule under non-AFR is defined using a plastic potential function ϕ_p independent of ϕ_y and thus reads

$$d\boldsymbol{\varepsilon}_p = \gamma \frac{\partial \phi_p}{\partial \boldsymbol{\sigma}} \tag{2}$$

where γ is the plastic multiplier and $d\boldsymbol{\varepsilon}_p$ is the incremental plastic strain tensor. If associated flow is assumed and the yield locus/potential function is homogeneous, the plastic multiplier corresponds to the increment of equivalent plastic strain $d\bar{\varepsilon_p}$. The derivation of the plastic multiplier for non-AFR, has been treated in detail by [24], where different strategies were proposed for an appropriate scaling of the incremental plastic strain tensor. The theoretically required scaling factor can be derived based on the principle of plastic work equivalence:

$$\phi_y d\bar{\varepsilon}_p = \boldsymbol{\sigma} : d\boldsymbol{\varepsilon}_p \tag{3}$$

using Euler's theorem

$$\boldsymbol{\sigma} : \frac{\partial \phi_p}{\partial \boldsymbol{\sigma}} = \phi_p \tag{4}$$

and substituting Eq. 2 into Eq. 3, γ becomes

$$\gamma = d\bar{\varepsilon}_p \frac{\phi_y}{\phi_p} \tag{5}$$

This simplifies to $\gamma = d\bar{\varepsilon}_p$ in case of associated flow rule. Inverting the equation the scaling factor is found as $\frac{\phi_p}{\phi_y}$

$$d\bar{\varepsilon}_p = \gamma \frac{\phi_p}{\phi_y} \tag{6}$$

Explicit numerical formulation

The implemented stress integration algorithm is based on the forward-Euler tangent cutting plane algorithm (TCPA) proposed by [21]. Following [24], the implementation uses the scaled simplified method, where the yield locus and potential are only scaled to intersect for uniaxial tension along the rolling direction. Safaei et al. [24] have shown

Table 1 Experimental stress-ratios and r-values for AA5042 by [22] and for AA6016 determined at IVP

Angle from rolling direction	0°	15°	30°	45°	60°	75°	90°	Biaxial
AA5042								
Stress-ratio	1.0000	1.0000	1.0174	1.0149	1.0174	1.0373	1.0448	1.1090
r-value	0.3840	0.1920	0.6500	1.0700	1.2990	1.2240	1.4360	0.9910
AA6016								
Stress-ratio	1.000	–	–	0.965	–	–	0.973	0.986
r-value	0.686	–	–	0.500	–	–	0.666	1.000

Table 2 Parameters for associated and non-associated flow rule for AA5042 and AA6016

	a	α_1	α_2	α_3	α_4	α_5	α_6	α_7	α_8
AA5042									
Yield ϕ_y	8	−0.8052	1.6285	0.1199	0.7976	1.0216	0.8131	0.7547	1.3230
Potential ϕ_p	14	−1.2243	1.8246	−1.0709	0.3568	1.0023	0.9091	0.9997	1.8108
AFR	8	0.5667	1.2335	0.9908	0.8969	0.9741	0.6567	0.9745	1.0808
AA6016									
Yield ϕ_y	6	0.9629	1.0656	0.9904	1.0168	1.0111	1.0360	1.0317	1.0682
Potential ϕ_p	4.5	0.9793	0.8937	0.9255	1.0271	1.0243	0.9712	0.8765	1.1713
AFR	4.5	0.9936	0.9023	0.8855	1.0448	1.0351	1.0376	0.8930	1.2502

with a number of tests, that this method has almost the same precision as the full scaled method shown in Eq. 6. The yield locus used in this work is Yld2000-2d as proposed by [4] The steps of the TCPA implementation are discussed in the following.

The n^{th} increment of the algorithm is initialized by updating the trial stress with an elastic increment:

$$\boldsymbol{\sigma}^n_{trial} = \boldsymbol{\sigma}^{n-1} + \boldsymbol{C} : d\boldsymbol{\varepsilon}^n \tag{7}$$

Here $\boldsymbol{C}$ is the fourth order elasticity tensor according to Hooke's law and $d\boldsymbol{\varepsilon}$ is the total strain increment. The latter is received from the main LS-DYNA-3D code as an input for the user-subroutine and is externally computed using the rate of deformation tensor $\boldsymbol{D}^n$ as follows:

$$d\boldsymbol{\varepsilon}^n = dt^n \cdot \boldsymbol{D}^n \tag{8}$$

where dt is the current time step. The trial stress is used to evaluate yield locus, plastic potential and yield stress

$$\begin{aligned} \phi^n_y &= \phi_y\left(\boldsymbol{\sigma}^n_{trial}\right) \\ \phi^n_p &= \phi_p\left(\boldsymbol{\sigma}^n_{trial}\right) \\ \sigma^n_y &= \sigma^n_y\left(\bar{\varepsilon}^n_p\right) \end{aligned} \tag{9}$$

and the yield condition is checked

$$g^n = \phi^n_y - \sigma^n_y \tag{10}$$

If g^n is less than zero, the step was indeed elastic and no plastic correction is necessary. Otherwise, an increment for the plastic multiplier $\Delta\gamma$ is evaluated

$$\Delta\gamma = \frac{g^n}{\frac{\partial\phi^n_y}{\partial\boldsymbol{\sigma}}\boldsymbol{C}\frac{\partial\phi^n_p}{\partial\boldsymbol{\sigma}} - \frac{\partial\sigma^n_y}{\partial\bar{\varepsilon}^n_p}} \tag{11}$$

and the total plastic corrector is updated: $\gamma = \gamma + \Delta\gamma$. This, in turn, is used to update the effective plastic strain and the total stress tensor as follows:

$$\begin{aligned} \bar{\varepsilon}^{n+1}_p &= \bar{\varepsilon}^n_p + \gamma \\ \boldsymbol{\sigma}^{n+1}_{trial} &= \boldsymbol{\sigma}^n_{trial} - \gamma\boldsymbol{C}\frac{\partial\phi^n_p}{\partial\boldsymbol{\sigma}^n_{trial}} \end{aligned} \tag{12}$$

Yield function, potential and hardening are updated using this new trial stress state and then the yield condition is checked again:

$$g^{n+1} = \phi^{n+1}_y - \sigma^{n+1}_y \leq TOL \tag{13}$$

The tolerance used in the implementation is $TOL = 1.0E-5$. If the condition is satisfied, all variables are updated for the next state. Otherwise, the process is repeated from

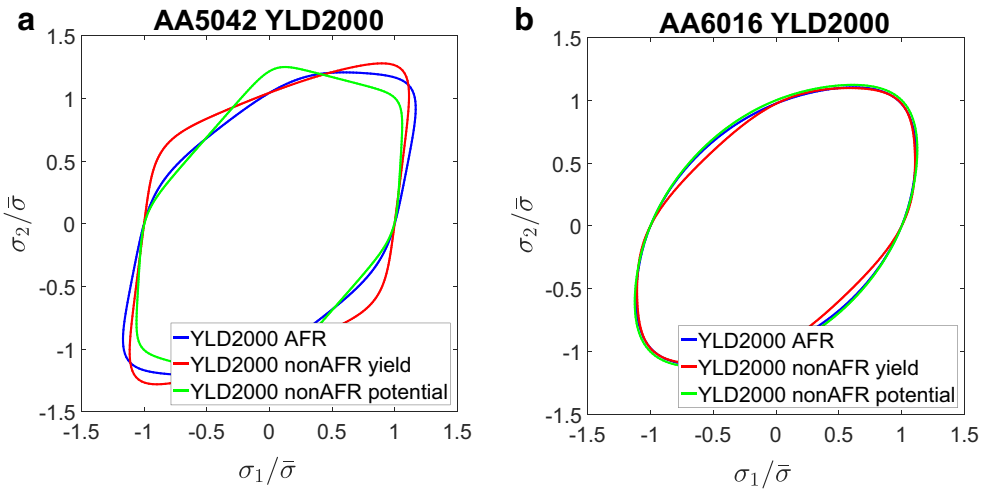

Fig. 1 Yield locus and potential shapes for (**a**) AA5042 and (**b**) AA6016

Table 3 Hardening curve parameters for AA5042 (Voce) and AA6016 (Hockett-Sherby)

	A	B	m	q
Voce	375.08	107.28	17.859	–
Hocket-Sherby	352.355	228.655	5.62	0.865

Eq. 11. Usually, no more than two sub-increments are needed due to small time steps in explicit FEM. The reader is referred to [21] for the derivation of the intermediate steps.

Implicit numerical formulation

The multi-stage return mapping algorithm, proposed by [32] has been chosen as the implicit numerical method. The algorithm executes a stepwise return mapping of the initially selected elastic trial stress $\boldsymbol{\sigma}^T$ onto the evolving yield locus and simultaneously satisfying normality and consistency conditions. The consistency condition for the k^{th} step during iteration n can be written as:

$$g_1(\gamma_k) = \phi_y(\boldsymbol{\sigma}_k) - \sigma_y\left(\bar{\varepsilon}_p^n + \gamma_k\right) - F_k = 0 \tag{14}$$

where F_k is constant to limit the current step and is ultimately set to zero at the end of the increment. The stress

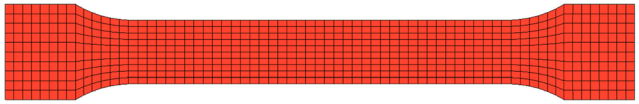

Fig. 3 Mesh for tensile test specimen

tensor at the k^{th} step is obtained by projecting the trial stress in the direction of the estimated normal of the plastic potential:

$$\boldsymbol{\sigma}_k = \boldsymbol{\sigma}_{trial}^n - \gamma_k \boldsymbol{C}\left(\frac{\partial \phi_p}{\partial \boldsymbol{\sigma}}\right)_k \tag{15}$$

This can be rewritten as a second vector function to be satisfied

$$\boldsymbol{g}_2(\gamma_k, \boldsymbol{\sigma}_k) = \boldsymbol{C}^{-1}\left(\boldsymbol{\sigma}_k - \boldsymbol{\sigma}_{trial}^n\right) + \gamma_k\left(\frac{\partial \phi_p}{\partial \boldsymbol{\sigma}}\right)_k = 0 \tag{16}$$

Linearizing the functions g_1 and g_2 delivers the following conditions:

$$g_1 + \Delta g_1 = g_1 + \frac{\partial \phi_y}{\partial \boldsymbol{\sigma}_k}\Delta\boldsymbol{\sigma}_k + \frac{\partial \sigma_y}{\partial \bar{\varepsilon}_p}\Delta\gamma_k = 0 \tag{17}$$

$$\boldsymbol{g}_2 + \Delta \boldsymbol{g}_2 = \boldsymbol{g}_2 + \frac{\partial \boldsymbol{g}_2}{\partial \boldsymbol{\sigma}_k}\Delta\boldsymbol{\sigma}_k + \frac{\partial \boldsymbol{g}_2}{\partial \bar{\varepsilon}_p}\Delta\gamma_k = 0 \tag{18}$$

Solving Eq. 18 for $\Delta\boldsymbol{\sigma}_k$ gives

$$\Delta\boldsymbol{\sigma}_k = -\boldsymbol{E}^{-1}\left(\boldsymbol{g}_2 + \Delta\gamma_k \frac{\partial \phi_p}{\partial \boldsymbol{\sigma}}\right) \tag{19}$$

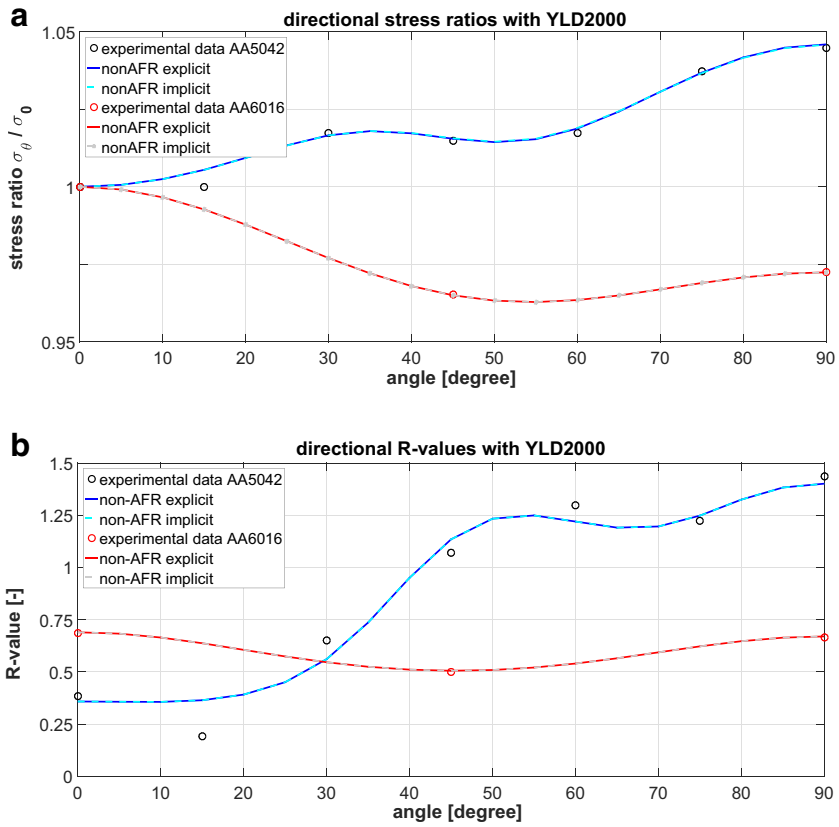

Fig. 2 Stress-ratio (**a**) and r-value (**b**) comparison for both AA5042 and AA6016 with YLD2000, AFR and non-AFR

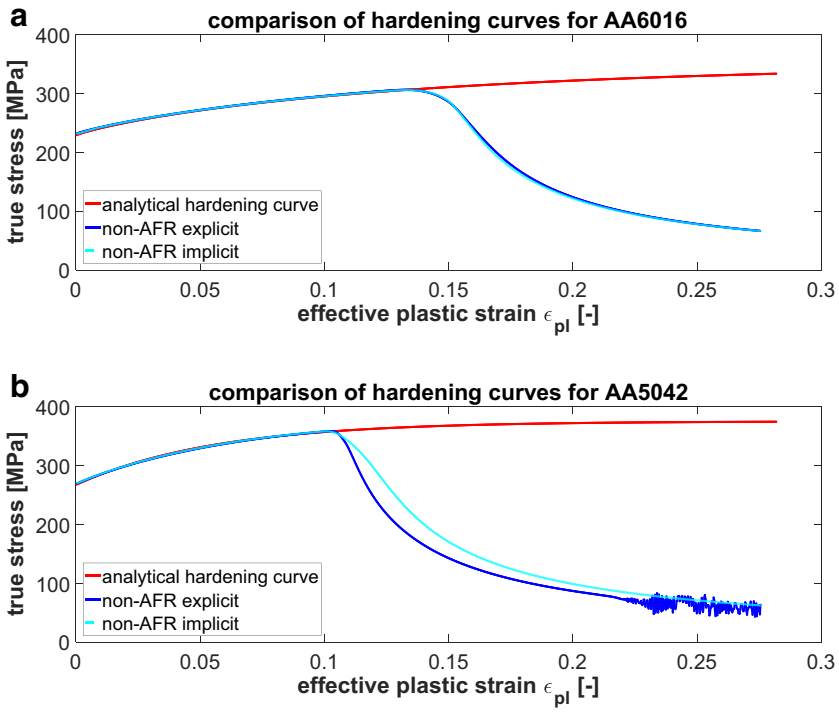

Fig. 4 Simulated tensile test result of AA6016 (**a**) and AA5042 (**b**)

with

$$\boldsymbol{E} = \boldsymbol{C}^{-1} + \gamma_k \frac{\partial^2 \phi_p}{\partial \boldsymbol{\sigma} \partial \boldsymbol{\sigma}} \tag{20}$$

Substituting Eq. 19 into Eq. 17 and rearranging an explicit expression for the subincrement size $\Delta\gamma_k$ is obtained:

$$\Delta\gamma_k = \frac{g_1 - \frac{\partial \phi_p}{\partial \boldsymbol{\sigma}} \boldsymbol{E}^{-1} \boldsymbol{g}_2}{\frac{\partial \phi_y}{\partial \boldsymbol{\sigma}} \boldsymbol{E}^{-1} \frac{\partial \phi_p}{\partial \boldsymbol{\sigma}} + \frac{\partial \sigma_y}{\partial \bar{\varepsilon}_p}} \tag{21}$$

The newly estimated equivalent plastic strain sub-increment is used to successively solve for the current equivalent strain, stress tensor and normal of the potential function. Iteration is then repeated until both g_1 and $\boldsymbol{g}_2$ are satisfied for the current substep, within a predefined tolerance (TOL).

Material characterization

Two aluminum alloys AA6016 and AA5042 have been considered in the scope of this work. R-values and stress ratios, have been measured for 0, 45, 90 degrees as well as the equi-biaxial stress ratio for AA6016. For AA5042, the same parameters measured at every 15 degrees from the rolling direction and equi-biaxial loading have been taken from [22]. All values are summarized in Table 1.

The Yld2000-2d model

The Yld2000-2d function, as proposed by [4], has been used for both yield function and plastic potential. The yield function Φ is defined as follows:

$$\Phi = \Phi' + \Phi'' = 2\sigma_y^a \tag{22}$$

with

$$\Phi' = \left|X_1' - X_2'\right|^a \tag{23}$$

$$\Phi'' = \left|2X_2'' + X_1''\right|^a + \left|2X_1'' + X_2''\right|^a \tag{24}$$

where X_i' and X_i'' are the principal values of the transformed stress tensors $\boldsymbol{X}'$ and $\boldsymbol{X}''$ which are in turn defined as

$$\boldsymbol{X}' = \boldsymbol{C}'\boldsymbol{T}\boldsymbol{\sigma} \text{ and } \boldsymbol{X}'' = \boldsymbol{C}''\boldsymbol{T}\boldsymbol{\sigma} \tag{25}$$

Table 4 Calculation times for the total of directional tests [min:sec]

	Explicit	Implicit	Difference	Difference [%]
AA5042 non-AFR	0:22	0:38	0:16	42.11
AA6016 non-AFR	0:27	0:34	0:07	20.59

Table 5 Calculation times for tensile tests in [min:sec]

	Explicit	Implicit	Difference	Difference [%]
AA5042 non-AFR	05:21	12:38	07:17	57.65
AA6016 non-AFR	05:50	09:10	03:20	34.55

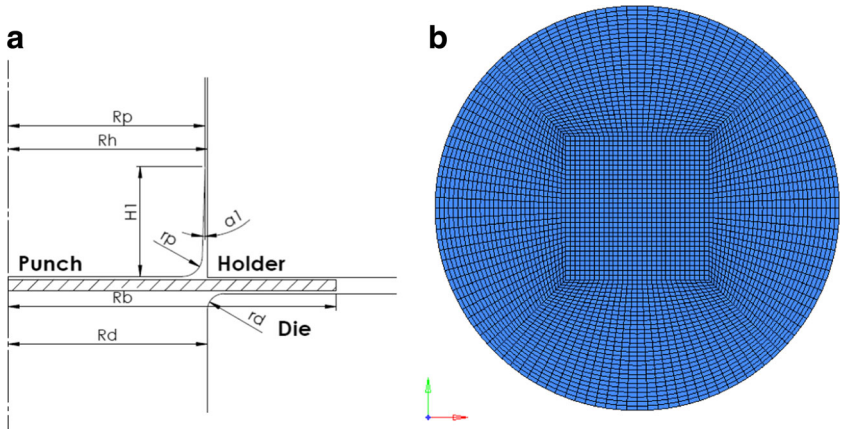

Fig. 5 (**a**) Schematics of tools for cup drawing for AA5042 and (**b**) corresponding mesh size

where $\boldsymbol{C}'$, $\boldsymbol{C}''$ and $\boldsymbol{T}$ represent transformation matrices in the function of the anisotropy parameters α_i. For a full description of the model, please refer to [4]. The derivative of this yield function is given by

$$\frac{\partial \Phi}{\partial \boldsymbol{\sigma}} = \frac{\partial \Phi'}{\partial \boldsymbol{X}'}\frac{\partial \boldsymbol{X}'}{\partial \boldsymbol{\sigma}} + \frac{\partial \Phi''}{\partial \boldsymbol{X}''}\frac{\partial \boldsymbol{X}''}{\partial \boldsymbol{\sigma}} \tag{26}$$

The Yld2000-2d yield function and potential were fitted using eight stress-ratios for the yield locus and eight r-values for the potential with AA5042. For AA6016, four stress-ratios were used for the yield locus (r-values assumed to be 1.0) and four r-values for the potential (stress ratios assumed to be 1.0). For the purpose of comparison, the AFR case is fitted additionally, using stress-ratios and r-values along 0, 45, 90 degrees from the rolling direction and biaxial state. The resulting α_i values and the exponents a are shown in Table 2. The non-integer exponent of $a = 4.5$ was found to give the best agreement with the experimental results for AA6016. The resulting yield locus and potential shapes are shown in Fig. 1. Note that for AA5042 yield locus and plastic potential differ significantly, whereas for AA6016 the two surfaces are closer in shape. These two materials are selected to test the numerical algorithms for different degrees of non-linearity as represented by the two models.

Isotropic hardening models

The hardening data for AA5042 are taken from [22]. The hardening curve for AA6016 is fitted using the Hockett-Sherby model. The analytical derivatives for Voce (27) and Hockett-Sherby (29) are given in the following. The identified model parameters are provided in Table 3.

$$\sigma_y = A - Be^{-m\bar{\varepsilon}_p} \tag{27}$$

$$\frac{\partial \sigma_y}{\partial \bar{\varepsilon}_p} = mBe^{-m\bar{\varepsilon}_p} \tag{28}$$

$$\sigma_y = A - Be^{-m\bar{\varepsilon}_p^q} \tag{29}$$

$$\frac{\partial \sigma_y}{\partial \bar{\varepsilon}_p} = qmBe^{-m\bar{\varepsilon}_p^q} \cdot \bar{\varepsilon_p}^{q-1} \tag{30}$$

Tensile tests and directional testing

The accuracy and efficiency of the two stress integration algorithms have been thoroughly tested under homogeneous uniaxial loading with two series of simulations. Firstly the ability of the models and implementations to properly capture anisotropy has been investigated using one-element tests in the different directions to the rolling direction. Secondly tensile test specimen has been meshed and simulated to validate the ability of the models to reproduce the stress-strain behavior properly.

The one-element test results for the explicit user-defined Material Subroutine (UMAT) are shown in Fig. 2 as stress-ratio or r-value vs. angle to the rolling direction for both materials. The simulated tensile test results are shown in Fig. 4. The mesh system used can be seen in Fig. 3. The results show that both integration schemes preform equivalently well under uniaxial loading for all tested models (Fig. 4).

As far as computational efficiency is concerned, the calculation times for both simulation series are shown in Tables 4 and 5. The One-element tests for every 5 degrees to the rolling direction were executed on a machine with Intel(R) Xeon(R) W3565 with 3.2GHz and 12 GB RAM. All calculations were performed on a single CPU with an

Table 6 Tool dimensions for cup drawing experiment [mm]

	Rp	Rd	Rh	Rb	rp	rd	H1	a1
AA5042	22.860	23.368	23.114	38.062	2.229	1.905	12.7	1.905

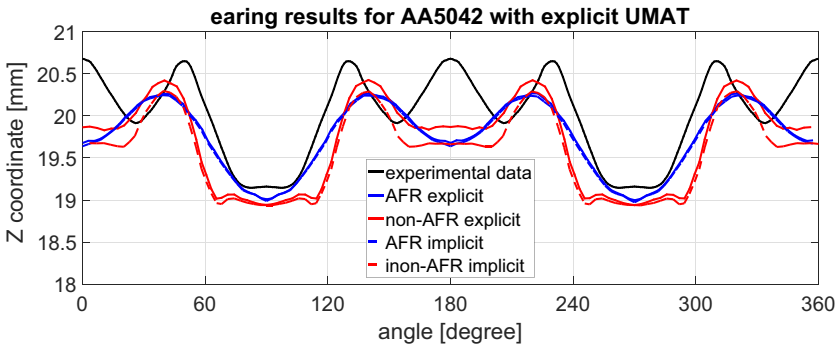

Fig. 6 Results of cup drawing experiment and simulation with AFR and non-AFR for AA5042 with explicit and implicit UMAT

enforced timestep of $1.5e-5$ using Belytschko-Tsay elements with seven integration points through the thickness. The Table shows the sum of 19 simulations (every 5 degrees to the rolling direction) for each case.

Table 5 compares the time needed for the explicit and implicit UMAT to compute the tensile test experiment on four CPUs (Intel(R) Xeon(R) W3565 3.20GHz with 12GB RAM) and a timestep of $1e-6$.

Cup drawing test

For the purpose of verification, a simulation model with higher complexity was chosen. For AA5042, a cup drawing experiment is simulated and compared to the experimental data obtained from [22]. The tool geometry is shown in Fig. 5a and the dimensions are listed in Table 6. For the blank, coarser meshes than those of Park and Chung are selected, as shown in Fig. 5b. The friction coefficient is 0.005, the blankholder force is $8.9kN$. Belytschko-Wong-Chiang shells as proposed by [7] are used with seven integration points through the thickness. The shell thickness is $0.21mm$. These earing profiles at the end of forming are compared for both the implicit and explicit implementation (see Fig. 6). The two algorithms do not deliver identical results, but the differences are in the order of magnitude of 0.15mm. With the same earing profiles compared to experimental data on the other hand, AFR based Yld2000-2d shows a noticeable difference compared to the experimentally observed profile. In order obtain the compatible accuracy with AFR, more accurate yield functions, e.g. Yld2004-16p ([2]) should be used. The calculation times are shown in Table 7. These simulations ran with four CPUs, explicit with a timestep of 1.0E-6 using LS-DYNA-3D-3D.

Table 7 Calculation times for cup drawing experiments in [h:min:sec]

	Explicit	Implicit	Difference	Difference [%]
AA5042 AFR	0:27:23	0:36:32	0:09:09	49.31
AA5042 non-AFR	0:21:08	1:10:38	0:49:30	70.21

Conclusions

The aim of this study is to systematically assess the efficiency of stress integration algorithms in the context of the numerically challenging non-AFR based constitutive models. Directional one-element tests, tensile tests as well as deep drawing tests have been used to compare the Euler-forward and Euler-backward algorithms in terms of accuracy and speed. It can be said that Euler-forward algorithm delivers comparable accuracy to the Euler-backward method. The difference in earing height and plastic strain remains generally low with only local peaks.

The directional tests carried out with different materials show that both algorithms are able of capturing the non-linearity presented by the models even if very different surfaces are used for the yield function and potential. It is noted that Euler forward integration scheme stays convergent, requiring at most three sub-increments making iterations expensive. This situation is also reflected by computations with nearly homogeneous strain distribution, such as tensile test experiments, even if to a lesser extent. The more realistic conditions presented by a cup drawing example, lead to an inhomogeneous distribution of the strains and in this case Euler-backward integration scheme delivers slower timings than Euler-forward scheme.

As far as the efficiency difference between AFR and non-AFR is concerned, it is noted that Euler-backward remains always slower for non-AFR calculations than AFR, whereas Euler-forward computes non-AFR models faster than AFR.

Compliance with Ethical Standards

Conflict of interests The authors declare that they have no conflict of interest.

References

1. Banabic D, Aretz H, Comsa DS, Paraianu L (2005) Theoretical plasticity of textured aggregates. Int J Plast 21:493–512
2. Barlat F, Aretz H, Yoon JW, Karabin ME, Brem JC, Dick RE (2005) Yielding description for solution strengthened aluminum alloys. Int J Plast 21:1009–1039
3. Barlat F, Becker RC, Hayashida Y, Maeda Y, Yanagawa M, Chung K, Brem JC, Lege DJ, Matsui K, Murtha SJ, Hattori S (1997) Yielding description for solution strengthened aluminum alloys. Int J Plast 13:385–401
4. Barlat F, Brem JC, Yoon JW, Chung K, Dick RE, Lege DJ, Pourboghrat F, Choi SH, Chu E (2003) Plane stress yield function for aluminum alloy sheets - part 1: theory. Int J Plast 19:1297–1319
5. Barlat F, Lege JD, Brem JC (1991) A six-component yield function for anisotropic materials. Int J Plast 7:693–712
6. Barlat F, Lian J (1989) Plastic behavior and stretchability of sheet metals. part i: a yield function for orthotropic sheets under plane stress conditions. Int J Plast 5:51
7. Belytschko T, Wong BL, Chiang HY (1992) Advances in one-point quadrature shell elements. Comput Methods Appl Mech Eng 96:93–107
8. Bishop JFW, Hill R (1951) A theory of plastic distortion of a polycrystalline aggregate under combined stresses. Phil Mag 42:414
9. Bland DR (1951) The associated flow rule of plasticity. J Mech Phys Solids 6:71–78
10. Brunig M (1999) Numerical simulation of the large elastic-plastic deformation behavior of hydrostatic stress-sensitive solids. Int J Plast 15:1237–1264
11. Brunig M, Obrecht H (1999) Finite elastic-plastic deformation behavior of crystalline solids based on a non-associated macroscopic flow rule. Int J Plast 14:1189–1208
12. Casey J, Sullivan TD (1985) Pressure dependency, strength-differential effect, and plastic volume expansion in metals. Int J Plast 1:39–61
13. Cazacu O, Flunkett B, Barlat F (2006) Orthotropic yield criterion for hexagonal closed packed metals. Int J Plast 22:1171–1194
14. Cazacu O, Ionescu IR, Yoon JW (2010) Orthotropic strain rate potential for the description of anisotropy in tension and compression of metals. Int J Plast 26:887–904
15. Drucker DC A more fundamental approach to plastic stress-strain relations. Proceedings of the First US National Congress of Applied Mechanics 1951, :487–491
16. Drucker DC (1959) A definition of stable inelastic material. J Appl Mech 26:101–106
17. Drucker DC (1964) On the postulate of stability of material in the mechanics of continua. J Mech 3:235–249
18. Hill R (1948) A theory of the yielding and plastic flow of anisotropic metals. Proc R Soc Lond 193:281
19. Hill R (1979) Theoretical plasticity of textured aggregates. Math Proc Camb 85:179–191
20. Li M, Richmond O (1997) Intrinsic instability and nonuniformity of plastic deformation. Int J Plast 8-9:765–784
21. Ortiz M, Simo JC (1986) An analysis of a new class of integration algorithms for elastoplastic constitutive relations. Int J Numer Methods Eng 23:353–366
22. Park T, Chung K (2012) Non-associated flow rule with symmetric stiffness modulus for isotropic-kinematic hardening and its application for earing in circular cup drawing. Int J Solids Struct 49:3582–3593
23. Paulino M, Yoon JW (2015) Study on yield function and plastic potential under non-associated flow for accurate prediction in cup drawing. Seel Research International 86:852–860
24. Safaei M, Yoon JW, Waele WD (2014) Study on the definition of equivalent plastic strain under non-associated flow rule for finite element formulation. Int J Plast 58:219–238
25. Spitzig WA, Richmond O (1984) The effect of pressure on the flow stress of metals. Acta Metallurgica 32:457–463
26. Stoughton TB (2002) A non-associated flow rule for sheet metal forming. Int J Plast 18:687–714
27. Stoughton TB, Yoon JW (2004) A pressure-sensitive yield criterion under a non-associated flow rule for sheet metal forming. Int J Plast 20:705–731
28. Stoughton TB, Yoon JW (2006) Review of drucker's postulate and the issue of plastic stability in metal forming. Int J Plast 22:391–433
29. Stoughton TB, Yoon JW (2008) On the existence of indeterminate solutions to the equations of motion under non-associated flow. Int J Plast 24:583–613
30. Yoon JH, Cazacu O, Yoon JW, Dick RE (2010) Earing predictions for strongly textured aluminium sheets. Int J Mech Sci 52:1563–1578
31. Yoon JW, Barlat F, Chung K, Pourboghrat F, Yang DY (2000) Earing predictions based on asymmetric nonquadratic yield function. Int J Plast 16:1075–1104
32. Yoon JW, Barlat F, Dick RE, Karabin ME (2004) Plane stress yield function for aluminum alloy sheets - part ii: Fe formulation and its implementation. Int J Plast 20:495–522
33. Yoon JW, Barlat F, Dick RE, Karabin ME (2006) Prediction of six or eight ears in a drawn cup based on a new anisotropic yield function. Int J Plast 22:174–193
34. Yoon JW, Dick RE, Barlat F (2011) A new analytical theory for earing generated from anisotropic plasticity. Int J Plast 27:1165–1184
35. Yoon JW, Lou Y, Yoon J, Glazoff MV (2014) Asymmetric yield function based on the stress invariants for pressure sensitive metals. Int J Plast 56:184–202
36. Yoon JW, Stoughton TB, Dick RE (2007) Earing prediction in cup drawing based on non-associated flow rule. AIP Conference Proceedings: Proceedings of 'Materials Processing and Design: Modeling, Simulation and Applications'